Optica Applicata, Vol. LVI, No. 1, 2026
DOI: 10.37190/oa/214547

Enhanced spectral resolution in optical fiber grating sensing using iterative reconstruction with error feedback and lowpass filtering

HANGTING YANG[1], DARYL TAN[1], KOK-SING LIM[1,*], ZHI CHAO ONG[2,3], HARITH AHMAD[1]

[1] Photonics Research Centre, University of Malaya, 50603 Kuala Lumpur, Malaysia

[2] Department of Mechanical Engineering, Faculty of Engineering, University of Malaya, 50603 Kuala Lumpur, Malaysia

[3] Centre of Research Industry 4.0 (CRI 4.0), Faculty of Engineering, University of Malaya, 50603 Kuala Lumpur, Malaysia

[*]Corresponding author: kslim@um.edu.my

This work introduces a novel iterative reconstruction algorithm that enhances low-resolution optical spectrum. The proposed method effectively recovers spectral features that are otherwise undetectable using low- to moderate-resolution interrogators. An adaptive low-pass filter is integrated into error feedback to effectively suppress noise while selectively preserving high-frequency spectral components during iterative reconstruction process. The algorithm's performance was validated using fiber grating Fabry–Perot interferometer (FPI) sensor spectrum with varying cavity lengths (4, 19, and 25 mm). Using high-resolution spectrum as references, the reconstructed spectrum demonstrated notable improvements, with reductions in ΔMAE (4 mm: –2.42%, 19 mm: –9.37%, and 25 mm: –32.51%) and ΔMSE (4 mm: –4.23%, 19 mm: –17.96%, and 25 mm: –61.22%) compared to the original low-resolution spectrum. Amongst filter methods, an "equiripple" low-pass filter is effective in enhancing the reconstructed spectrum by suppressing noise, resulting in reduced spectral errors (ΔMAE = –6.49%; ΔMSE = –12.97%). The proposed algorithm offers a practical and computationally efficient solution for recovering lost spectral details, particularly in the high-frequency region with minimal error. This capability is especially valuable for enhancing the performance of low-resolution interrogators, allowing their reconstructed spectrum to exhibit characteristics comparable to those obtained with high-resolution systems.

Keywords: Fabry–Perot interferometry, optical fiber sensing, spectrum interrogation, spectrum reconstruction.

1. Introduction

Optical fiber gratings (OFG)-based sensors such as intrinsic optical fiber Fabry–Perot interferometer (FPI) have revolutionized distributed sensing applications such as precise strain [1,2] and temperature sensing [3,4] as well as chemical [5] and biomedical diagnostics [6] due to their inherent advantages: immunity to electromagnetic interference, chemical resistance, and high sensitivity to physical parameters (*e.g.*, strain, temperature, and vibration). These sensors rely on the wavelength-dependent reflection properties of FPIs to detect changes in their environment [7,8].

OFG spectrum exhibits a dense comb-like narrow-band interference pattern under spectral interrogation. Visibility of the interference pattern is highly dependent on the spectral resolution of the spectral interrogation system [9,10]. The spectral features particularly in the high frequency region are often unmeasurable by the low-resolution spectral interrogation system. On the other hand, the actual features of the OFG spectrum can be obtained by using high-resolution spectrum interrogation system [11]. Nevertheless, these devices are expensive and limited to laboratory uses, which have hampered the application of OFG sensing in field deployment. Therefore, it is crucial to introduce algorithmic methods to improve demodulation precision of the OFG spectrum under hardware constraints.

Various spectrum reconstruction algorithms have been developed and applied for optical fiber sensing. For instance, DIAS *et al.* proposed a spectral reconstruction technique based on a Bayesian model framework to characterize measured spectrum from long-period fiber gratings [12]. This approach offers a promising avenue for spectrum reconstruction in low-cost interrogation systems. Conversely, numerous studies have utilized neural networks (NNs) for spectrum reconstruction, achieving high-resolution and precise demodulation by reconstructing spectrum from original data with limited sampling points [13]. However, NNs demand extensive training datasets and significant computational resources, which restricts their applicability in real-time or resource-constrained environments [14].

Iterative reconstruction (IR) is a reconstruction model for low-resolution spectrum. It minimizes the error between measured and reconstructed signals through multiple iterative steps. It is particularly effective in refining both noise levels and signal detail characteristics [15,16]. The IR algorithm has been widely used in computed tomography (CT) imaging to reduce image artefacts [17], and has also proven effective in enhancing optical signals [18] with lesser processing time and minimal instrumentation [19].

In this paper, we demonstrate the use of IR algorithm to recover lost spectral features of fiber-grating Fabry–Perot interferometers (FPIs). The algorithm operates within a spectral reconstruction framework that iteratively refines the spectrum based on error feedback convergence. An "equiripple" low-pass filter is incorporated to the error feedback to effectively suppress noise while preserving high-frequency spectral components. To validate the proposed method, spectral reconstruction was performed on FPI spectrum with varying cavity lengths (4, 19, and 25 mm), allowing assessment of the algorithm's robustness across spectrum with different interference fringe densities and free spectral ranges (FSRs). With high-resolution spectrum used as a reference, the differences in mean absolute error (ΔMAE) and mean square error (ΔMSE) between the low-resolution and reconstructed spectrum served as quantitative indicators of the algorithm's performance.

2. Method

To reconstruct the high-resolution spectrum effectively, the gathering of low resolution and reference high resolution data is imperative. A data collection setup (refer to Fig. 1) was employed to generate sensing signals, which were utilized to reconstruction the high-resolution spectrum. In the experimental setup, FPI was inscribed using femtosecond laser (Indylit 10 SH, Litilit, Lithuania: 515 nm, 450 fs, repetitive rate of 80 kHz, pulse energy of 600 nJ) direct writing method. Two parallel lines were inscribed with length of 10 μm across the SMF-28 fiber core to form the FPI reflectors, and inter-distance between two reflectors were determined by adjusting the six-axis nano-positioning flexure stage (MAX683, Thorlabs Inc., USA). Different FPI spectrum (obtained from FPI with three different cavity lengths: 4, 19, and 25 mm, respectively) were obtained using optical spectrum analyzer (AQ6317B, Ando (Yokogawa), Japan) with a resolution of 10 pm. On the other hand, a high-resolution optical spectrum analyzer (AP2051A, APEX Technology, France) was utilized to acquire the FPI spectrum at the wavelength resolution of 1.44 pm which later serve as the reference spectrum for the analysis of the reconstructed spectrum.

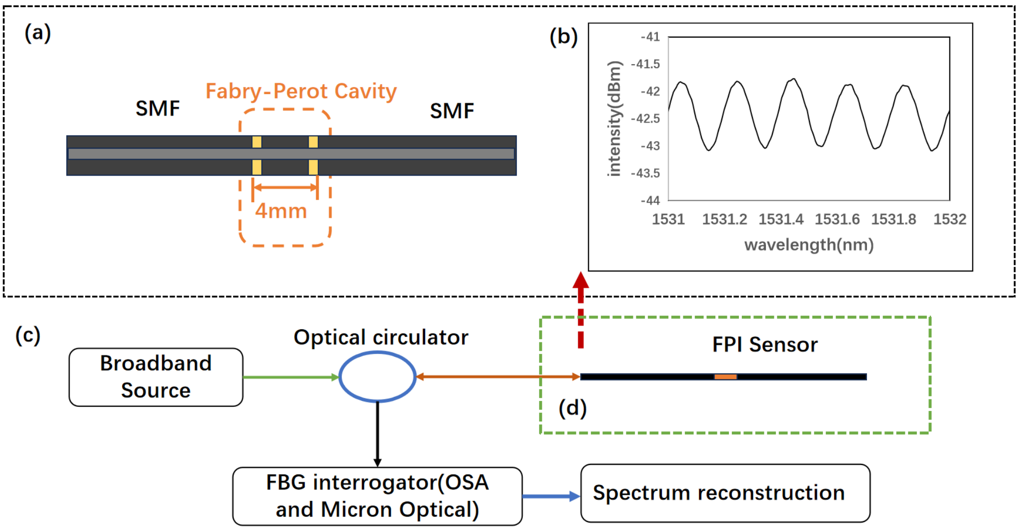

Fig. 1. (a) Illustration of an FPI with a cavity length *d*. (b) Reflection spectrum of the sensor. (c) Illustration of the experimental setup to perform spectrum reconstruction from the obtained FPI spectrum via proposed algorithm.

Figure 2 illustrates the comprehensive workflow of the IR algorithm designed to enhance the resolution of the low-resolution OFG spectrum. The process begins by registering the initial measured spectrum as the "observed spectrum, O(λ)". This spectrum serves as the baseline against which improvements are assessed throughout the reconstruction process. Simultaneously, an estimated observed spectrum, denoted as $\hat{O}_n(\lambda)$,

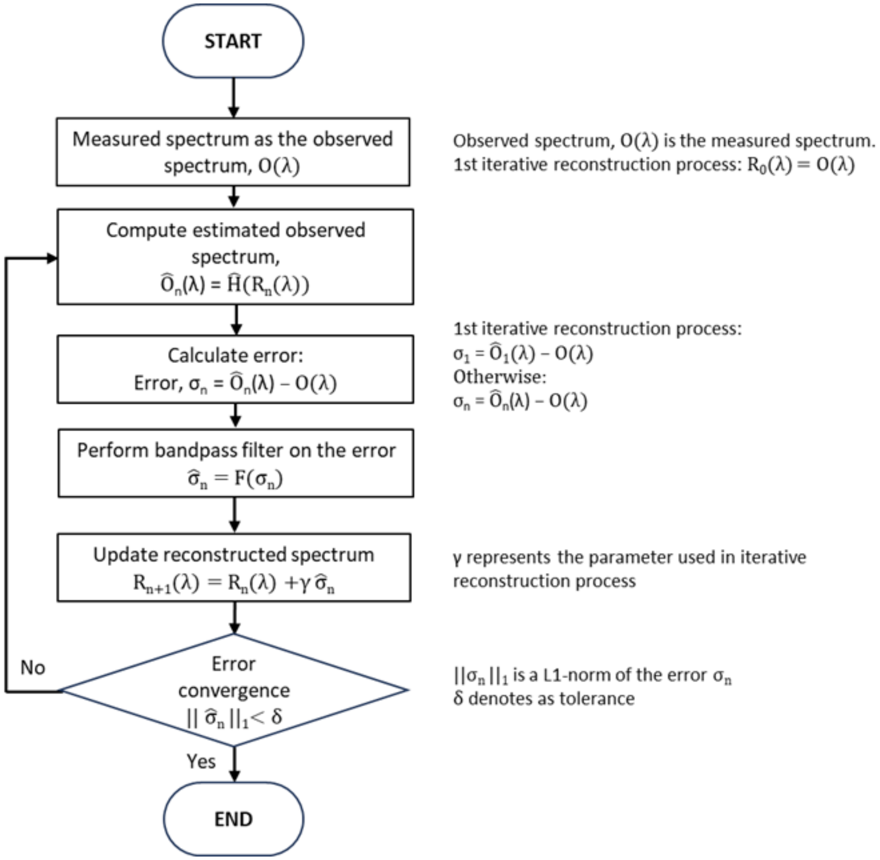

Fig. 2. Work flow of the spectrum reconstruction algorithm.

is computed based on current iteration. This estimation aims to approximate the observed spectrum as closely as possible. The core of the reconstruction process involves calculating the error σ_n which quantifies the deviation between the observed spectrum, and the estimated spectrum, $\sigma_n = \hat{O}_n(\lambda) - O_n(\lambda)$, to refine the errors in the relevant frequency region, notably in the low frequency region, using a lowpass filter. This step ensures that only significant spectral components contribute to the reconstruction, effectively reducing noise and enhancing features critical to accurate spectrum estimation.

The reconstructed spectrum for the next iteration, $R_{n+1}(\lambda)$, is then updated using the formula:

$$R_{n+1}(\lambda) = R_n(\lambda) + \gamma\hat{\sigma}_n \tag{1}$$

Here, γ represents the learning rate, a crucial parameter controlling the rate of convergence error feedback. A carefully chosen learning rate ensures that the algorithm makes substantial progress without overshooting, thereby maintaining stability and accuracy. The iterative loop continues, progressively refining the reconstructed spectrum until the convergence error feedback criterion is met. Specifically, the process halts when the L_1-norm of the error, $\|\sigma_n\|_1$, falls below a predefined minimum tolerance, δ. This condition ensures the reconstruction has reached an acceptable level of accuracy, balancing precision and computational efficiency.

The design of low-pass filters can be achieved using various methods, among which the "equiripple" design method is an effective optimization technique for designing finite impulse response (FIR) low-pass filters. The "equiripple" design allows for achieving a filter of minimal order given specified passband frequency, stopband frequency, and the desired passband and stopband ripple [20]. The key to this design method lies in utilizing window functions and minimizing the maximum error, thereby ensuring the filter's performance meets the specified criteria in the defined frequency ranges. The design of an FIR "equiripple" filter aims to minimize the maximum deviation (ripple) between the desired frequency response and the actual frequency response over specified frequency bands [21].

The output of the FIR filter can be expressed as a weighted sum of the input signal, with filter coefficients generally denoted as $F[n]$:

$$y[n] = \sum_{k=0}^{N-1} F[k]\,x[n-k] \tag{2}$$

In the Eq. (2) where $y[n]$ represents the output frequency of the filter, while $x[n]$ denotes the input frequency. The filter is characterized by its coefficient's $F[k]$, which have a length of L, where L is the order of the filter, indicating the number of filter coefficients used in the filtering process.

Mean absolute error (MAE) and mean squared error (MSE) are calculated to indicate the differences between low-resolution measured spectrum (or reconstructed spectrum) to reference spectrum as stated in Eqs. (3) and (4). Furthermore, the differences of MAE and MSE (*i.e.*, ΔMAE and ΔMSE) are used to provide quantitative evaluation of the reconstruction quality of the spectrum:

$$\mathrm{MAE}_{\text{low-res/recon}} = \frac{1}{m}\sum_{i=1}^{m}\left|v_{i,\,\text{low-res/recon}} - v_{i,\,\text{ref}}\right| \tag{3}$$

$$\mathrm{MSE}_{\text{low-res/recon}} = \frac{1}{m}\sum_{i=1}^{m}\left(v_{i,\,\text{low-res/recon}} - v_{i,\,\text{ref}}\right)^2 \tag{4}$$

$$\Delta\mathrm{MAE} = \frac{\mathrm{MAE}_{\text{recon}} - \mathrm{MAE}_{\text{low-res}}}{\mathrm{MAE}_{\text{low-res}}} \tag{5}$$

$$\Delta\mathrm{MSE} = \frac{\mathrm{MSE}_{\text{recon}} - \mathrm{MSE}_{\text{low-res}}}{\mathrm{MSE}_{\text{low-res}}} \tag{6}$$

where $\mathrm{MAE}_{\text{low-res}}$, $\mathrm{MAE}_{\text{recon}}$, $\mathrm{MSE}_{\text{low-res}}$, and $\mathrm{MSE}_{\text{recon}}$ represent MAE and MSE for low-resolution measured spectrum and reconstructed spectrum, respectively. m denotes the total number of data point, $v_{i,\text{low-res}}$, $v_{i,\text{recon}}$, and $v_{i,\text{ref}}$ are denoted as values of low-resolution measured spectrum, reconstructed spectrum, and reference spectrum, respectively, at particular index, i. The reference spectrum refers to the high-resolution spectrum.

3. Result and discussion

To comprehensively evaluate the performance of the reconstruction algorithm, we selected FPIs of different lengths for spectral collection. This selection not only accounts for variations in experimental conditions but is also intended for testing the algorithm's stability and accuracy for various different optical spectral characteristics. The algorithm is tested for different FPI configurations (*i.e.*, 4, 19, and 25 mm), to verify its applicability under a wider range of real-world application scenarios. Figure 3 shows

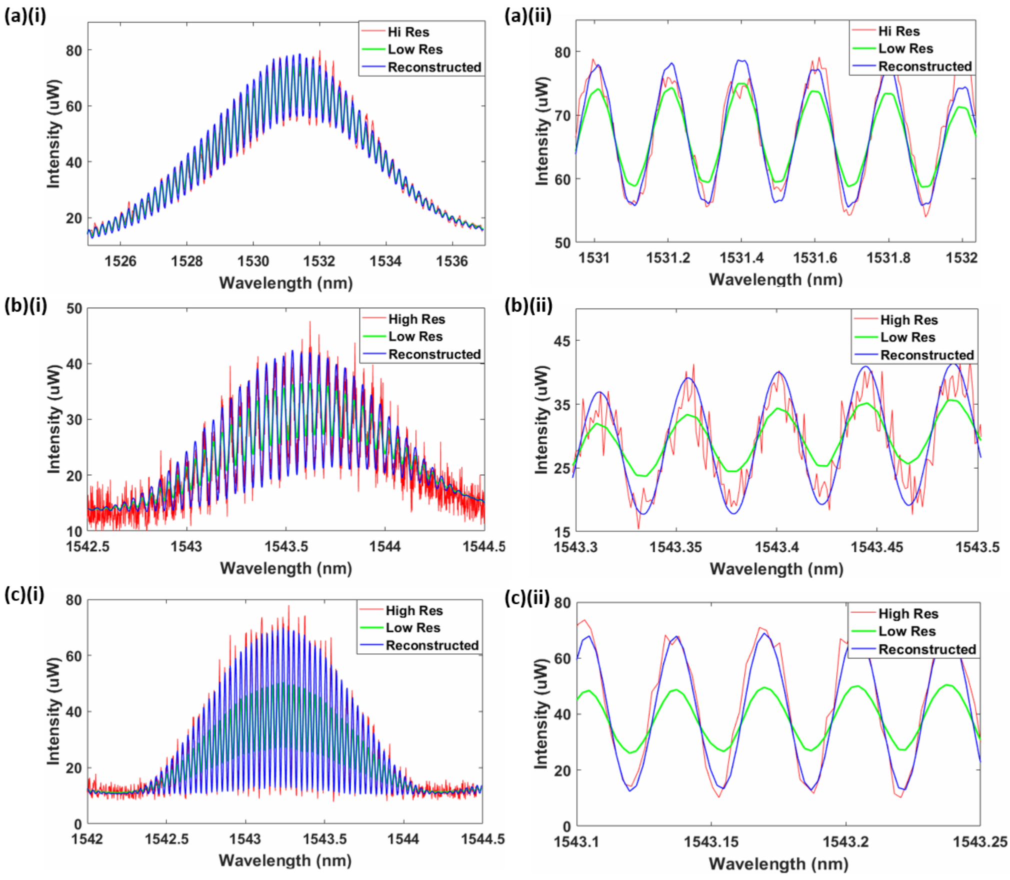

Fig. 3. Spectra represent the high-resolution (red line), low-resolution (green line) and reconstructed FPI spectrum (blue line), respectively, under different FPI cavities: (a) 4 mm, (b) 19 mm, and (c) 25 mm. (a)(ii), (b)(ii), and (c)(ii) show the interference pattern in detail for FPI with Fabry–Perot cavity of 4, 19, and 25 mm, respectively with learning rate of 0.001.

Table 1. Comparison of MAE and MSE for FPIs with varying cavity lengths.

FPI	$MAE_{low\text{-}res}$ [μW]	MAE_{recon} [μW]	ΔMAE [%]	$MSE_{low\text{-}res}$ [μW]	MSE_{recon} [μW]	ΔMSE [%]
4 mm	1.660	1.620	–2.42	4.749	4.548	–4.23
19 mm	2.600	2.353	–9.37	11.222	9.206	–17.96
25 mm	3.489	2.355	–32.51	26.248	10.179	–61.22

the result of reconstructed spectral data corresponding to FPI lengths of 4, 19, and 25 mm in the comparison with the low-resolution spectrum and reference high resolution spectrum. Table 1 compares the MAE and MSE of low-resolution measured spectrum and reconstructed spectrum for FPIs with different cavity lengths. Significant reduction in MAE and MSE can be observed for all the spectrum (*i.e.*, ΔMAE: 4 mm = –2.42%, 19 mm = –9.37%, and 25 mm = –32.51%; ΔMSE: 4 mm = –4.23%, 19 mm = –17.96%, and 25 mm = –61.22%). The improvement is particularly obvious for spectrum with higher cavity length (smaller FSR and higher frequency components in the spatial frequency spectrum). This comparison highlights the effectiveness of the reconstruction algorithm, where reduction in MAE and MSE indicate the close alignment of wavelengths and peak intensities between the reconstructed and high-resolution spectrum validates the algorithm's ability to accurately capture the essential features of the original high-resolution data, reinforcing its accuracy and reliability in spectral reconstruction tasks.

Selection of an appropriate learning rate for the IR system is important as it significantly influences the convergence performance and accuracy of the model. The learning rate is a critical parameter influencing the performance of reconstruction models. The lower is the learning rate, the slower is the system convergence and the smaller is the error of the result, but the larger is the reconstruction error. During the model debugging process, it has been observed that while the learning rate significantly influences the magnitude of the error, determining the optimal learning rate to achieve the desired reconstruction results remains a challenge. In this context, we employed a threshold -based early stopping method to prevent both overfitting and underfitting during the reconstruction process. The combination of the threshold and the learning rate settings perfectly aligns with the requirements of our system. Figure 4 presents three potential scenarios that the system may encounter: underfitting, appropriate fitting, and overfitting.

The reconstructions produced by the algorithm exhibited varying degrees of distortion, with noticeable offsets present in the peak portions. After each iteration, a digital low-pass filter is applied in the spatial frequency domain to suppress high-frequency noise. The cutoff frequency is adaptively set according to the estimated noise band, with 3 dB passband ripple and 7 dB stopband attenuation. Iteration proceeds until the change in mean absolute error (MAE) falls below 10^{-4} or a maximum iteration limit is reached. This process effectively reduces high-frequency noise while preserving the spectral features, with all implementations performed in MATLAB (R2020a). Two contrasting examples of these initial reconstructions are depicted in Fig. 5, in which

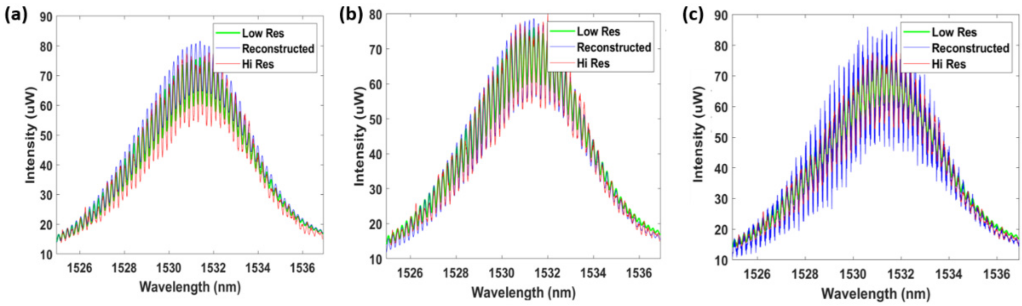

Fig. 4. Spectrum of FPI with 4 mm-cavity length under different reconstruction scenarios: (a) underfitting (error tolerance = 9.7×10^{-3}), (b) appropriate fitting (error tolerance = 9.7×10^{-4}), and (c) overfitting reconstruction (error tolerance = 8.2×10^{-5}) with learning rate of 0.001.

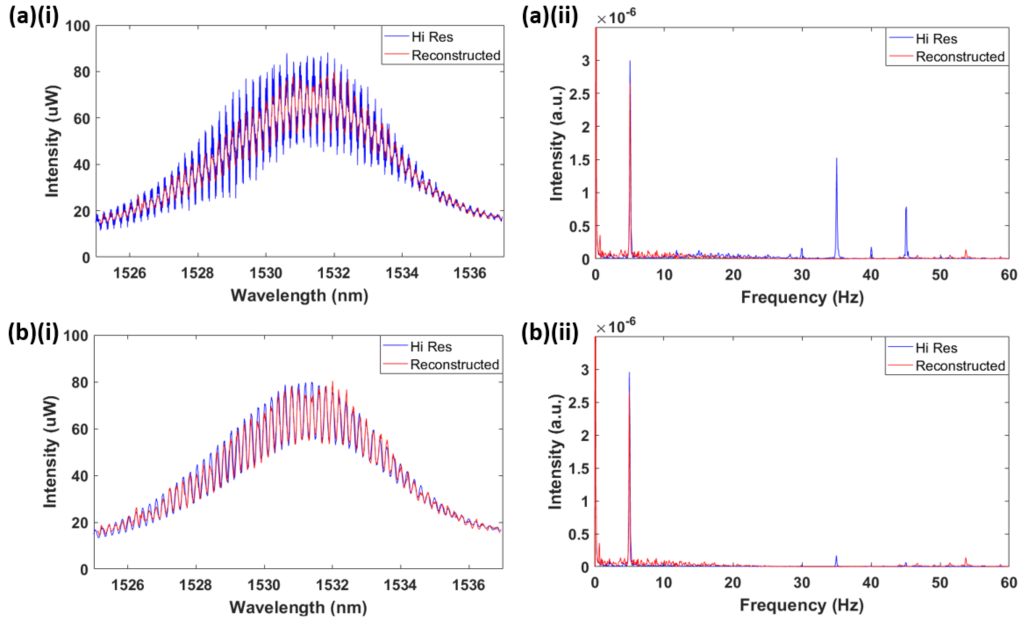

Fig. 5. Reconstructed spectrum from the FPI with 4 mm-cavity under different criteria: (a) without filter, and (b) with low-pass FPI "equiripple" filter under same reconstructed parameter using learning rate of 0.001. The FPI spectrum in frequency domain shows different scenarios: (a)(ii) existence of unwanted reconstructed signal as noise without the use of low-pass filtering; and (b)(ii) suppression of unwanted reconstructed signal with low-pass filtering.

the presence of noise in the reconstructed frequency range can be observed, while the low and high-resolution frequency ranges remain unaffected. The noise observed in Fig. 5(a)(ii) can indirectly contribute to the growth of undesired noise in the reconstructed spectrum as shown in Fig. 5(a)(i). In contrast, Fig. 5(b)(i) and 5(b)(ii) present the outcomes after applying the low-pass FIR "equiripple" filter, clearly demonstrating a suppression of unwanted reconstructed spectrum and subsequently provides a significant improvement in noise levels. Both the reconstruction errors, MAE and MSE of the spectrum have been reduced (MAE: 1.7323 μW → 1.5889 μW; MSE: 5.2257 μW → 4.3202 μW).

A comparative analysis of iterative counts and reconstruction time for different filter methods is illustrated in Fig. 6, and comparisons in both MAE and MSE are listed in Table 2. Experimental findings show that among the tested filter types, the "equiripple" filter consistently achieved the lowest reconstruction errors, with MAE/MSE values of 1.620 μW/4.548 μW, 2.353 μW/9.145 μW, and 2.355 μW/10.179 μW with the use of FPI with cavity length of 4, 19, and 25 mm, respectively. This indicates superior noise suppression and spectral fidelity compared with least-square, Kaiser, Butterworth,

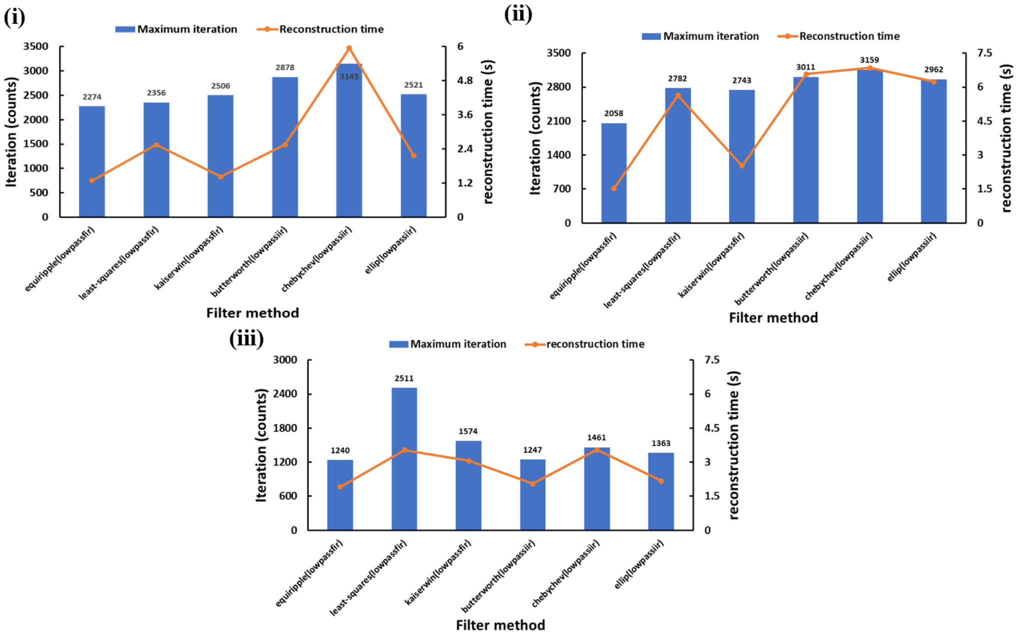

Fig. 6. Plot of maximum iterations and reconstruction times against different filters for the spectra of (i) 4 mm, (ii) 19 mm, and (iii) 25 mm of cavity length FPI, respectively.

Table 2. Comparison in MAE and MSE for different filters used in spectrum reconstruction.

Type of FPI		Equiripple*	Least-square	Kaiserwin	Butterworth	Chebychev	Ellip
4 mm	MAE [μW]	1.620	1.648	1.701	1.636	1.629	1.646
	MSE [μW]	4.548	4.710	5.044	4.637	4.561	4.541
19 mm	MAE [μW]	2.353	2.4194	2.4133	2.3621	2.3741	2.3583
	MSE [μW]	9.1452	9.7915	9.7743	9.272	9.3712	9.2408
25 mm	MAE [μW]	2.3549	2.5366	2.6503	2.8501	3.3311	2.6035
	MSE [μW]	10.1786	11.8822	13.299	16.5129	20.3313	13.3736

*Filtering method used in reconstruction algorithm in this work.

Chebyshev, and elliptic filters. The "equiripple" filter's sharp transition band and controlled ripple contribute to more accurate fringe preservation, making it the most effective choice for the FPI signal reconstruction. However, it is notable that "equiripple" excels in computational efficiency, with a reconstruction time of only 1.83 s, significantly faster than other methods (least-squares = 3.54 s, kaiserwin = 3.06 s, butterworth = 2.06 s, chebychev = 3.54 s, ellip = 2.17 s). The "equiripple" is able to meet the predetermined reconstruction convergence with a relatively low iteration counts of 1240 as compared to other methods under same reconstruction settings. Hence, it indicates that "equiripple" not only maintains low error levels but also offers faster convergence and significantly improved computational efficiency. Therefore, "equiripple" stands out as the optimal choice when balancing accuracy and computational performance.

Figures 7(a)–(c) show the performance of the reconstruction algorithm that was evaluated by analyzing the reconstruction results (*i.e.*, maximum iteration and reconstruction time) of 4, 19, and 25 mm FPI spectrum under different learning rates. The analysis of the reconstruction results reveals a clear relationship between learning rate, reconstruction time, and maximum iteration. As the learning rate decreases from 0.5 to 0.001, both the reconstruction time and the number of iterations increase significantly. For instance, in 4mm-cavity length FPI, the reconstruction process undergoes 5 iterations with a reconstruction time as low as 0.02 s under a learning rate of 0.5. When the algorithm is set to a learning rate of 0.001, the spectrum reconstruction requires 2274 iterations with reconstruction time of 1.29 s to achieve the convergence error

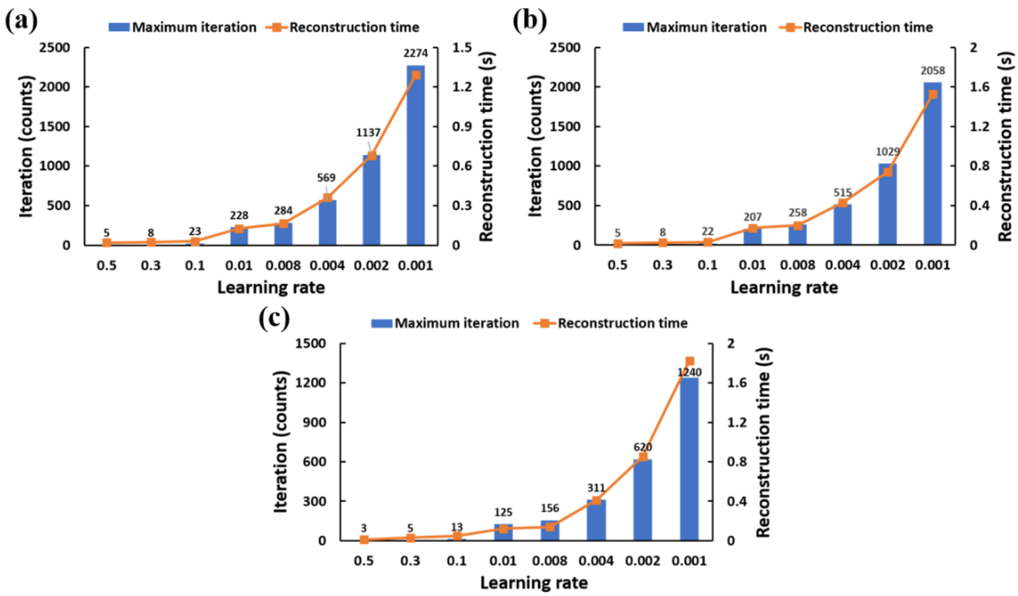

Fig. 7. Maximum iteration and reconstruction time *versus* learning rate. Different plots representing the reconstruction results obtained from three FPIs with different cavity lengths: (a) 4 mm, (b) 19 mm, and (c) 25 mm.

feedback criteria. This trend demonstrates that higher learning rates (*e.g.*, 0.5, 0.3) prioritize computational efficiency, enabling faster reconstruction with fewer iterations, which is ideal for applications requiring quick results. On the other hand, lower learning rates (*e.g.*, 0.001, 0.002) provide more precise convergence but at the cost of significantly increased computational time and resources. The choice of learning rate should therefore be guided by the specific needs of the task, balancing the trade-off between speed and accuracy. For time-sensitive applications, higher learning rates are preferable, while scenarios demanding higher precision may benefit from lower learning rates despite the longer processing time.

For a spectrum reconstruction system, the reconstruction time is an important evaluation criterion. Of course, the reconstruction time is directly proportional to the total number of data points of the spectral data that needs to be reconstructed. Since the reconstruction increases the total number of data point and resolution, the reconstruction ratio is represented by the resolution enhancement factor N. The enhancement factor, N is fully applicable to the reconstruction of FPI spectrum and the value of N is calculated as follows:

$$N = \frac{\text{Total number of data point (reconstructed spectrum)}}{\text{Total number of data point (low-resolution spectrum)}} \tag{7}$$

Figure 8 shows the performance of different N. Under a fixed maximum iteration of 500, the reconstruction error (MAE) of the spectrum gradually increases as the reconstruction precision N increases. This is primarily due to the fact that higher reconstruction precision leads to greater data complexity, involving more data points and more intricate features, which in turn require more computational resources (*e.g.*, iteration counts) to achieve accurate fitting. As shown in Fig. 8, for lower-resolution spectrum (*e.g.*, $N = 2$), a total iteration of 500 is sufficient to allow the algorithm to reconstruct the spectrum's features to be similar to the high-resolution spectrum, as the lower number of data points aligns well with the model's complexity. However, for higher-resolution spectrum (*e.g.*, $N = 20$), the fixed 500 iterations are insufficient

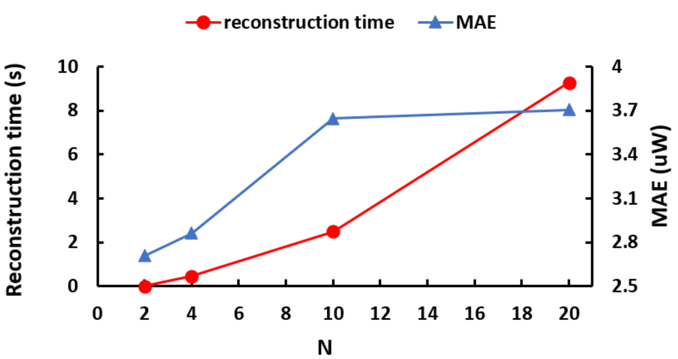

Fig. 8. The MAE and reconstruction time *versus* enhancement factor N under reconstruction settings (learning rate = 0.001, maximum iteration = 500, and without a pre-set value for the error tolerance).

to capture the additional details and features, resulting in increased errors. Therefore, to reduce errors, it is recommended to either increase the iteration count or optimize the algorithm parameters to better accommodate higher-resolution spectral data. This approach would enhance the algorithm's ability to handle more complex data while maintaining high reconstruction accuracy.

4. Conclusion

This study presents an iterative reconstruction (IR) algorithm that enhances OFG-based spectrum measured by low to moderate-resolution spectral interrogators. By incorporating a low-pass filter to reduce noise, the algorithm produces a refined reconstructed spectrum that closely resemble high-resolution spectrum. The observed reductions in mean absolute error (ΔMAE: 4 mm = –2.42%, 19 mm = –9.37%, and 25 mm = –32.51%) and mean squared error (ΔMSE: 4 mm = –4.23%, 19 mm = –17.96%, and 25 mm = = –61.22%) after the reconstruction process confirm the algorithm's effectiveness in improving spectral clarity and accuracy. Amongst filter methods, an "equiripple" low-pass filter is effective in enhancing the reconstructed spectrum by suppressing noise, resulting in reduced spectral errors (ΔMAE = –6.49%; ΔMSE = –12.97%). This method enables enhanced spectral resolution without requiring high-resolution spectral scanning. Furthermore, it highlights the potential of the IR algorithm as a reliable solution to maintain demodulation accuracy for low to moderate-resolution interrogation devices.

Acknowledgements
Authors acknowledge the University Malaya Research University Grant, University of Malaya [RU001-2025B].

References

[1] PAN X.P., YANG H.E., LIU S.R., WANG B., GAO M.M., GUO Q., CHEN Q.D., SUN H.B., YU Y.S., *High sensitivity fiber optic strain sensor based on CFBG-FPI and Vernier effect*, Journal of Lightwave Technology, **41**(21), 2023: 6831-6837. https://doi.org/10.1109/JLT.2023.3291413

[2] ZHANG X., ZHENG Z., WANG H., XIANG P., *Strain transfer analysis of a four-layer embedded fiber optic sensing model in an elastic state*, Surface Review and Letters, **32**(03), 2025: 2450117. https://doi.org/10.1142/S0218625X24501178

[3] AN G., LIU L., HU P., JIA P., ZHU F., ZHANG Y., LIU J., XIONG J., *Probe type TFBG-excited SPR fiber sensor for simultaneous measurement of multiple ocean parameters assisted by CFBG*, Optics Express, **31**(3), 2023: 4229-4237. https://doi.org/10.1364/OE.481948

[4] LI X., LI Y., WANG C., JIN W., FU G., FU X., BI W., *High-sensitivity optical fiber probe for simultaneous measurement of chloride ions and temperature*, Applied Optics, **62**(36), 2023: 9430-9436. https://doi.org/10.1364/AO.500182

[5] JAHARUDIN N.A.N., TAN D., CHOLAN N.A., UDOS W., RAMALINGAM N., NGAJIKIN N.H., LIM K.S., AHMAD H., *Optofluidic sensor for iron detection based on inline Fabry–Perot interferometer fabricated by femtosecond laser pulses and selective etching*, IEEE Sensors Journal, **25**(5), 2025: 8324 -8332. https://doi.org/10.1109/JSEN.2025.3530448

[6] GHASEMI M., OH J., JEONG S., LEE M., BOHLOOLI DARIAN S., OH K., KIM J.K., *Fabry–Perot interferometric fiber-optic sensor for rapid and accurate thrombus detection*, Biosensors (Basel), **13**(8), 2023: 817. https://doi.org/10.3390/bios13080817

[7] LIU T., WU M., RAO Y., JACKSON D.A., FERNANDO G.F., *A multiplexed optical fibre-based extrinsic Fabry-Perot sensor system for in-situ strain monitoring in composites*, Smart Materials and Structures, **7**(4), 1998: 550. https://doi.org/10.1088/0964-1726/7/4/016

[8] RAO Y.-J., *Fiber Bragg grating sensors: Principles and applications*, [In] Grattan K.T.V., Meggitt B.T., [Eds.], *Optical Fiber Sensor Technology: Devices and Technology*, Springer, Boston, MA, 1998: 355-379. https://doi.org/10.1007/978-1-4615-5787-6_11

[9] LU C., CUI J., CUI Y., *Reflection spectra of fiber Bragg gratings with random fluctuations*, Optical Fiber Technology, **14**(2), 2008: 97-101. https://doi.org/10.1016/j.yofte.2007.09.007

[10] YUE Z., ZHENG D., ZOU X., XIE C., PENG Y., *Large dynamic range interrogation technique for fiber-optic interferometric sensor based on AWG and deep learning algorithm*, IEEE Sensors Journal, **24**(1), 2024: 278-286. https://doi.org/10.1109/JSEN.2023.3329299

[11] BORISOV Y.S., NIZAMETDINOV A.M., IVANOV O.V., CHERTORIYSKIY A.A., *Measurement of spectra of fiber Bragg gratings by tuning the wavelength of a laser diode*, Optics and Laser Technology, **151**, 2022: 108048. https://doi.org/10.1016/j.optlastec.2022.108048

[12] DIAS B., SANTOS P., JORGE P.A.S., DE ALMEIDA J.M.M.M., COELHO L.C.C., *Spectral reconstruction and Bayesian model framework for characterization of long period fiber gratings*, IEEE Instrumentation & Measurement Magazine, **24**(5), 2021: 56-62. https://doi.org/10.1109/MIM.2021.9491007

[13] XU H., CHEN S., REN S., HOU X., PENG H., WANG G., ZHANG Y., *High-resolution spectrum reconstruction of cascaded FBG-FPI sensor in resource-constrained environments*, IEEE Sensors Journal, **24**(7), 2024: 11878-11885. https://doi.org/10.1109/JSEN.2024.3365546

[14] CHEN S., REN S., YANG J., YAO F., YANG Q., WANG L., WANG G., HUANG M., *Reconstruction of Fabry-Perot interferometric sensor spectrum from extremely sparse sampling points using dense neural network*, IEEE Photonics Technology Letters, **34**(24), 2022: 1337-1340. https://doi.org/10.1109/LPT.2022.3216909

[15] HERMAN G.T., *Fundamentals of Computerized Tomography: Image Reconstruction from Projections*, 2nd Ed., Springer, 2009. https://doi.org/10.1007/978-1-84628-723-7

[16] GEYER L.L., SCHOEPF U.J., MEINEL F.G., NANCE J.W., BASTARRIKA G., LEIPSIC J.A., PAUL N.S., RENGO M., LAGHI A., DE CECCO C.N., *State of the art: Iterative CT reconstruction techniques*, Radiology, **276**(2), 2015: 339-357. https://doi.org/10.1148/radiol.2015132766

[17] WILBERS A., BIGURI A., SCHILLINGS J., LOOS J., *Application of iterative reconstruction algorithms to mitigate CT-artefacts when measuring fiber reinforced polymer materials*, Polymer (Guildf), **177**, 2019: 120-130. https://doi.org/10.1016/j.polymer.2019.06.004

[18] WANG W., ZOU D., LI Z., SUI Q., CAO Z., LU C., LI F., LI Z., *Optical single sideband signal reconstruction based on time-domain iteration*, Journal of Lightwave Technology, **39**(8), 2021, 2319-2326. https://doi.org/10.1109/JLT.2021.3050855

[19] PALTAUF G., VIATOR J.A., PRAHL S.A., JACQUES S.L., *Iterative reconstruction algorithm for optoacoustic imaging*, Journal of the Acoustical Society of America, **112**(4), 2002: 1536-1544. https://doi.org/10.1121/1.1501898

[20] SINGH T.C., KUMAR M., *Digital FIR filter designs*, 2021 Asian Conference on Innovation in Technology (ASIANCON), 2021: 1-5.

[21] HOSSAIN K., AHMED R., HAQUE A., RAHMAN M.T., *A review of digital FIR filter design in communication systems*, International Journal of Science and Research (IJSR), **10**(2), 2021: 1380-1391. https://doi.org/10.21275/sr21221133619

Received July 26, 2025
in revised form November 4, 2025